Time-Domain Modelling of Pulsed Photoconducting Sources - Part II Characterization of an LT GaAs Bow-Tie Antenna

Bernardis, Arturo Fiorellini; Sberna, Paolo Maria; Bueno, Juan; Zhang, Huasheng; Llombart, Nuria; Neto, Andrea

DOI
10.1109/TAP.2023.3236763

Publication date
2023

Document Version
Final published version

Published in
IEEE Transactions on Antennas and Propagation

Citation (APA)
Bernardis, A. F., Sberna, P. M., Bueno, J., Zhang, H., Llombart, N., & Neto, A. (2023). Time-Domain Modelling of Pulsed Photoconducting Sources - Part II: Characterization of an LT GaAs Bow-Tie Antenna. *IEEE Transactions on Antennas and Propagation*, *71*(3), 2536-2545. https://doi.org/10.1109/TAP.2023.3236763

Time-Domain Modelling of Pulsed Photoconducting Sources—Part II: Characterization of an LT GaAs Bow-Tie Antenna

Arturo Fiorellini Bernardis, *Graduate Student Member, IEEE*, Paolo Maria Sberna, Juan Bueno, Huasheng Zhang, *Graduate Student Member, IEEE*, Nuria Llombart, *Fellow, IEEE*, and Andrea Neto, *Fellow, IEEE*

***Abstract*— Drude's description of the response of low-temperature gallium arsenide to optical pulse excitation is used to evaluate the components of a time-domain Norton equivalent circuit of a photoconductive antenna (PCA) source. The saturation of the terahertz (THz) radiated power occurring at large optical excitation levels was previously associated by the scientific community to radiation and charge screening of the bias. With the present circuit, we are able to model accurately the measured saturation as only due to the EM feedback from the antenna to the bias. The predicted THz radiated power is shown to match very accurately the measurements when the circuit is combined with an accurate description of the experimental conditions and the modeling of the THz quasi-optical (QO) channel.**

***Index Terms*— Equivalent circuit, photoconductive antennas (PCAs), terahertz (THz), THz radiated power, THz sources, THz technology.**

I. Introduction

In THE last 30 years, the interest in terahertz (THz) technology, sparked by the many possible applications such as spectroscopy and imaging, has given rise to the emergence of time-domain sensing instruments relying on photoconducting (PC) antenna sources [1], [2], [3], [4].

For such sources, a distinctive limiting effect has been the saturation of the THz power output emerging at large optical excitations of the photoconductive substrate [5], [6], [7], [8]. Several equivalent circuits have been proposed in [9] and [10], with [9] being the most representative and [10] a recent review. In [11], some of the present authors introduced a procedure, based on the rigorous application of the electromagnetic equivalence theorem, that allows to characterize the THz spectrum time evolutions of PC sources, with a Norton equivalent circuit containing only one equivalent current generator. This is in contrast with previous works [10] that resorted to equivalent circuits with more generators, of which at least one was tuned by means of experiments. The Norton circuit from [11] prescribes the time evolution for the voltage and the current in the load even in the case of high optical excitation, overcoming the limitations of the frequency-domain circuit in [12].

With this contribution (which closely follows [13]), we explicitly introduce in the Norton circuit components the description of the physical processes involved in the generation, the motion, and the recombination of the carriers in a photoconductive device manufactured with a substrate of low-temperature grown gallium arsenide (LT GaAs). Specifically, a PC broadband antenna is excited by a pulsed femtosecond laser, is fed by a constant bias voltage, and radiates into a silicon (SI) lens. A Drude–Lorentz model [14] is used to describe the time evolution of the carrier density change induced by the optical excitation [15], [16]. The current and the voltage in the radiation resistance load that represents the antenna are obtained following the time-stepped procedure presented in [11]. In turn, the time stepping is here specified to include a double convolution integral that accounts for the history of the material and its dispersive behavior. Once the voltage and currents are known, the corresponding Fourier transforms can be evaluated. The analysis in the frequency domain is in indeed well suited for the characterization of the propagation of the generated THz signals in the lens and the analysis of the quasi-optical (QO) system leading to the receiver (RX) or the power meter in an experiment.

The complete procedure, including the circuit and the QO channel, is validated by comparing the expected power and spectra with data collected from a measurement campaign. The measured and simulated results agree exceptionally well also for intense optical excitations.

This article is structured as follows. In Section II, we demonstrate how to establish the constitutive current–voltage relations for the pulsed PC gap starting from semiconductor physics. In Section III, we present the equivalent circuit to analyze the photoconductive antenna, as well as the method to solve it by incremental time evolutions. In Section IV, we describe the design of the experimental setup and the acquired data. Finally, Section V shows the comparison between the power and spectra predicted by the model against the measurements.

II. Pulsed Photoconducting Gap

The photoconductive antenna (PCA) antennas considered here are printed on an LT GaAs layer. This layer is grown

Manuscript received 14 September 2021; revised 10 June 2022; accepted 14 September 2022. Date of publication 19 January 2023; date of current version 6 March 2023. This work was supported by the European Research Council (ERC) Starting Grant Lens Antenna Arrays for Coherent THz Cameras (LAA-THz-CC) under Grant 639749. *(Corresponding author: Andrea Neto.)*

The authors are with the Faculty of Electrical Engineering, the Delft University of Technology, 2628 CD Delft, The Netherlands (e-mail: A.Neto@tudelft.nl).

Color versions of one or more figures in this article are available at https://doi.org/10.1109/TAP.2023.3236763.

Digital Object Identifier 10.1109/TAP.2023.3236763

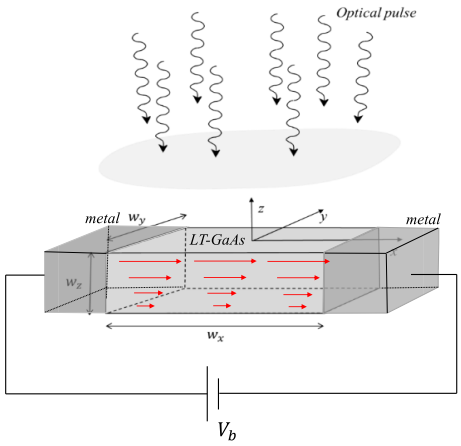

Fig. 1. Optically excited, biased, active PC volume.

on a substrate of semi-insulating GaAs, while a thin layer of aluminum-doped GaAs separates them, to avoid conduction currents flowing from the LT layer to the semi-insulating layer. We identify the active LT portion of the PC source with a volume Vol $= W_x W_y W_z$, as shown in Fig. 1, where the $\hat{z}$-axis is orthogonal to the dielectric volume and the $\hat{x}$- and $\hat{y}$-axis are parallel and transverse to the biasing electric field due to the voltage V_b, respectively.

A. Electrically Small Gap

The time (t)-dependent local volumetric current density is generated by the optical pulses and the bias in every observation point $\vec{r} = (x, y, z)$ within the volume of the PC domain (Fig. 1). A conduction current in the LT membrane can flow only along the direction imposed by the bias, taken here as $\hat{x}$. The current density, red arrows in Fig. 1, is distributed over a thickness, W_z, in the order of a couple of micrometers. As discussed in [12], the THz current distribution in z can be considered uniform after having being averaged over the thickness. The gaps whose lateral, $W_x W_y$, dimensions are also small: they are small with respect to the distribution of the optical beam so that can be assumed uniform on the gap and they are small with respect to the wavelengths represented in the THz spectrum. Accordingly, the electric current distribution dependence on x and y can also be further assumed to be uniform in the gap, as in [12]. Similarly, we will consider also the electric field, $\vec{e}_g(t)$, to be uniform in the gap. With the notation introduced in [11], $\vec{e}_g(t) = \vec{e}_b - \vec{e}(t)$, where $\vec{e}(t)$ represents the THz component of the field. These simplifying hypotheses for the electric current and the electric field distribution simplify the analysis justifying the use of a lumped circuit representation for the current and voltage across the PC gap in the THz band.

B. Constitutive Relations

A theoretical description of the photoconductive currents induced in semiconductors under pulsed lasers is presented in [16]. A portion of the electron charges that are freed at a time t'' will still be able to move in the conduction band at a later time t. Congruently, with the assumption that the electric current is constant for all observation points $\vec{r}$ in the PC gap volume, also the charge volume density, $n(\vec{r}, t, t'')$, dependence can be averaged and assumed constant and not dependent on the observation point within Vol. As detailed in the Appendix, the charge density generated at time t'' can be indicated as $g_{\text{gen}}(t'')$

$$g_{\text{gen}}(t'') = Ae^{-4ln2\frac{t''}{\tau_p^2}} \tag{1}$$

where the amplitude A is expressed as

$$A = \eta_{\text{opt}} \frac{\tilde{P}_L}{hf_c} \frac{T}{\tau_p} \sqrt{\frac{4ln2}{\pi}} \frac{1}{\text{Vol}} \tag{2}$$

where A accounts for the average laser power, $\tilde{P}_L$, arriving at the antenna, the repetition period (T) and the duration (τ_p) of the pulses, as well as the optical central frequency, f_c, and Planks constant h. A number of efficiency factors, such as spatial optical distributions (in x, y, z), the reflection at the dielectric air interface, and the energy needed to free one electron [12], are all included in a global optical efficiency, η_{opt}. This latter is a design parameter that with an accurate design was brought to $\eta_{\text{opt}} \approx 35\%$ in the experiment discussed in Section III. $\tilde{P}_{\text{opt}} = \eta_{\text{opt}} \tilde{P}_L$ is the average optical power absorbed in the gap, corresponding to the optical power $\tilde{P}_{\text{opt}}$ considered in [11].

In the following, $n_{\text{ave}}(t, t'')$ will indicate the average charge density in the volume that has become available at time t'' by (1) and still available at time t because the charges have not recombined. It can be expressed as [16]

$$n_{\text{ave}}(t, t'') = g_{\text{gen}}(t'') h_{\text{GaAs}}(t - t'') \left[\frac{1}{m^3 s}\right] \tag{3a}$$

$$h_{\text{GaAs}}(t) = e^{-\frac{t}{\tau_c}} \tag{3b}$$

where $h_{\text{GaAs}}(t)$ is the material impulse response and τ_c is the carrier recombination constant. In view of this notation, the average electric current density in the gap can be expressed as

$$\vec{j}_{\text{partial}}(t, t'') = q_e n_{\text{ave}}(t, t'') \vec{v}_e(t, t'') \tag{4}$$

where q_e is the electron charge $q_e = 1.610^{-19}\ C$ and $\vec{v}_e(t, t'')$ is the velocity of the charge distribution at time t. This latter velocity does not depend only on the electric field at t but also from previous times t''. Drude's model [14], [15], [16] introduces an explicit dependence of the velocity, $\vec{v}_e(t, t'')$, on the time t'' when the charge distribution has become available. Accordingly, the velocity depends on the electric field that was present in the time interval from the instant that the charge was created, t'', up to the instant, t, when the velocity is being observed

$$\vec{v}_e(t, t'') = \frac{q_e}{m_{e,\text{GaAs}}} \int_{t''}^{t} e^{-\frac{t-t'}{\tau_s}} \vec{e}_g(t') dt'. \tag{5}$$

In (5) τ_s is the relevant scattering time, while $m_{e,\text{GaAs}} = m_e 0.067$ and m_e are the effective masses of an electron in the conduction band of GaAs and free space, respectively. Substituting in (4) the definition of the velocity as a function of the electric field, (5), one obtains

$$\vec{j}_{\text{partial}}(t, t'') = n_{\text{ave}}(t, t'') \frac{q_e^2}{m_{e\text{GaAs}}} \int_{t''}^{t} e^{-\frac{t-t'}{\tau_s}} \vec{e}_g(t') dt'. \tag{6}$$

The current in (6) decreases as time goes on because of the recombination of electrons and holes: $e^{-(t-t''/\tau_c)}$. The total

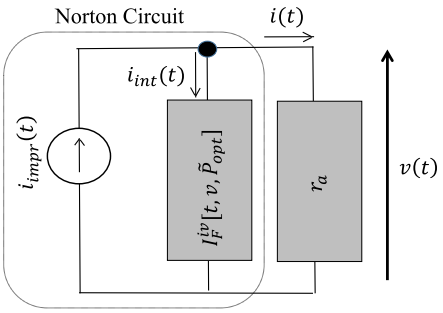

Fig. 2. Time-domain Norton equivalent circuit with antenna resistance load.

current density present in the gap, $\vec{j}$, at the instant of time t can be expressed as the superposition of all contributions generated during the optical pulse

$$\vec{j}(t) = \int_{-\infty}^{t} \vec{j}_{\text{partial}}(t, t'')dt''. \tag{7}$$

The explicit double integral expression for the total current density is then

$$\vec{j}(t) = A\frac{q_e^2}{m_{e\text{GaAs}}} \cdot \int_{-\infty}^{t} e^{-4ln2\frac{t''^2}{\tau_p^2}} \int_{t''}^{t} e^{-\frac{t-t'}{\tau_s}} \vec{e}_g(t')dt' e^{-\frac{t-t''}{\tau_c}} dt''. \tag{8}$$

This equation is equivalent to those in [16]. Integrating over the cross section (W_y, W_z) of the semiconductor block, the net total current flowing in the PC gap can be expressed as

$$i(t) = \iint_{W_y W_z} \vec{j}(t) \cdot \hat{x} dy dz = W_y W_z j_x(t). \tag{9}$$

Similarly, integrating the electric field along the gap gives rise to a voltage drop across the gap $v_g(t)$

$$v_g(t) = \int_{Wx} \vec{e}_g(t) \cdot \hat{x} dx = e_{g,x}(t) W_x \tag{10}$$

so that the relation between actual net currents and voltages over the gap can be expressed as

$$i(t) = A\frac{q_e^2}{m_e}\frac{W_y W_z}{W_x} \times \int_{-\infty}^{t} e^{-4ln2\frac{t''^2}{\tau_p^2}} \int_{t''}^{t} e^{-\frac{t-t'}{\tau_s}} v_g(t')dt' e^{-\frac{t-t''}{\tau_c}} dt''. \tag{11}$$

Equation (11) represents a deterministic relation between voltage and current, valid for the general case in which the total number of free electrons is determined by a pulsed laser (Gaussian τ_p), and the semiconductor can be described by a scattering time τ_s from Drude's model and a recombination time τ_c. Moreover, it represents the constitutive relation between $v_g(t)$ and $i(t)$ that was described in [11, eq. (13)] as $i(t) = I_F^{iv}[t, v_g, t_0, \tilde{P}_{\text{opt}}]$. Here, we assumed that $t_0 = 0$.

C. Time-Domain Equivalent Circuit

A Norton equivalent circuit representing the problem under investigation is shown in Fig. 2. The constitutive relation here appears as a component in parallel with load, which represents the antenna impulse response. As shown in [11], the equivalent current generator is obtained using the material constitutive relation with the constant voltage bias V_b as follows:

$$i_{\text{impr}}(t) = A\frac{q_e^2}{m_{e\text{GaAs}}}\frac{W_y W_z}{W_x} \times \int_{-\infty}^{t} e^{-4ln2\frac{t''^2}{\tau_p^2}} \int_{t''}^{t} e^{-\frac{t-t'}{\tau_s}} V_b dt' e^{-\frac{t-t''}{\tau_c}} dt''. \tag{12}$$

The antenna's impulse response, in electrically long, broadband antennas, can be approximated as Dirac's delta when one neglects late time reflections from the ends, as discussed in [11] at the end of Section V. For these configurations, it is then legitimate to represent the antenna load as a real radiation resistance r_a in Fig. 2.

Solving the circuit leads to a system of two equations and two unknowns, $i(t)$ and $v(t)$, that can be solved numerically, using a time-stepped evolution as in [11]

$$i(t) = i_{\text{impr}}(t) - i_{\text{int}}(t). \tag{13}$$

Substituting (12) in (13) and the constitutive relations in terms of the impulse response of the gap to specify $i_{\text{int}}(t)$, the load current can be expressed as

$$i(t) = \frac{q_e^2}{m_e}\frac{W_y W_z}{W_x} \times A\int_{-\infty}^{t} e^{-4ln2\frac{t''^2}{\tau_p^2}} \int_{t''}^{t} e^{-\frac{t-t'}{\tau_s}} \left(V_b - v(t')\right)dt' e^{-\frac{t-t''}{\tau_c}} dt'' \tag{14a}$$

which must be verified simultaneously with the constitutive relation of the antenna load

$$v(t) = i(t) r_a. \tag{14b}$$

The set of (14) can be solved by stepping in the time.

Fig. 3 shows the temporal evolution of the current $i(t)$ and the voltage drop across the gap, $v_g(t) = V_b - v(t)$, predicted by the circuit for three different laser power levels, a bias of $V_b = 30\ V$, and an antenna radiation impedance $r_a = 70\ \Omega$. The material and laser parameters are given in Table I. The gap is assumed to be characterized by $W_x = W_y = 10\ \mu$m, $W_z = 2\ \mu$m, and to be excited with optical efficiency (discussed in

TABLE I
MAIN LASER AND MATERIAL PARAMETERS FOR THE EXPERIMENT

Laser Parameters	
Wavelength	$\lambda = 780nm$
Pulse FWHM	$\tau_p = 100fs$
Repetition rate	$T = 12.5ns$
Maximum Average Laser Power	$\tilde{P}_L = 240\ mW$
Material Parameters	
Carrier recombination time	$\tau_c = 300fs$
Relative Dielectric constant	$\varepsilon_r = 12.96$
Carrier effective mass	$m_{eGaAs} = 0.067 \cdot m_e$
Plane wave reflection coefficient	$\Gamma = 0.5477$
Absorption coefficient	$\alpha = 1/\mu m$
Scattering time	$\tau_s = 8.5\ fs$

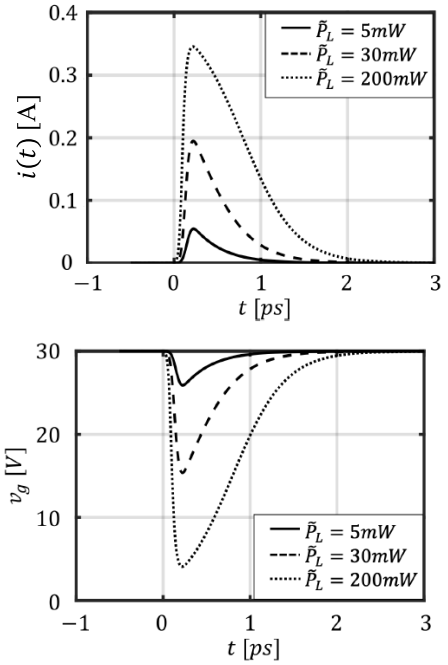

Fig. 3. Temporal evolution of current, $i(t)$, and voltage, $v_g(t)$, across the photoconductive gap for a bias voltage of $V_b = 30$ V, a radiation resistance of $r_a = 70\ \Omega$, and three different optical excitation $\tilde{P}_L = 5$, 30, and 200 mW, and optical efficiency $\eta_{\text{opt}} = 0.35$.

the appendix) $\eta_{\text{opt}} = 0.35$. Fig. 3 shows that the increase of the optical excitation does not lead to a linear increase in the amplitude of current or voltage. The time signature of both the current and the voltage on the gap changes as the optical power increases.

This is the mark of the saturation that was previously observed in the literature, for which a dedicated "screening" component had been introduced. The circuit in Fig. 2 includes the screening while maintaining a standard single-source Norton structure. The energy spectrum radiated in the lens can be expressed as

$$E_{\text{rad}}(f) = Re\{Z_a(f)\}|I(f)|^2 \tag{15}$$

where Z_a represents the impedance of the antenna and $I(f) = \text{FT}[i(t)]$ indicates the Fourier transform of the current, $i(t)$.

The antenna radiation impedance, $Z_a(f)$, for the antenna that in Section III is used in the experimental verification is simulated as a function of the frequency using the full-wave EM simulation tool CST [17]. The simulated impedance is shown in Fig. 5. Since most of the power is contained in the band from 100 GHz $\rightarrow$ 1 THz, where the real part is significantly larger than the imaginary part, the impedance can be approximated as constant, $Z_a(f) \simeq 70\ \Omega$.

The energy spectrum is shown in Fig. 4 for three different optical excitations. An increase of laser power clearly corresponds to higher overall energy spectra. However, it is apparent that for larger optical excitations, the largest enhancement of the radiated energy is concentrated in the lower frequencies.

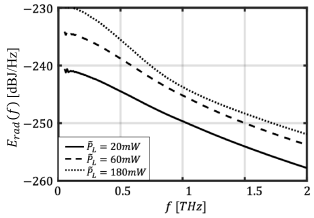

Fig. 4. Energy spectra radiated by the feed into the silicon lens antenna evaluated using the methodology presented in this article. The curves refer to three different optical excitations, $\eta_{\text{opt}} = 0.35$.

The corresponding average power radiated in the lens can be expressed as

$$\tilde{P}_{\text{rad}} = \frac{2}{T}\int_0^\infty Re\{Z_a(f)\}|I(f)|^2 df \tag{16}$$

where T is the period of the pulse repetition and the integration is performed with unilateral spectra. This power can be calculated independently on the QO efficiency of the channel from transmitter (TX) to TX.

III. Experimental Validation

The validity of the model is checked by measuring a bow-tie photoconductive antenna. The same bow-tie antenna was partially investigated in [12], and we fully characterize it in this measurement campaign. These measurements are performed in the THz Laser Laboratory of the Terahertz Sensing Group, TU Delft.

A. Photoconductive Antenna Design

The bow-tie antenna under test consists of a metallization printed over a substrate of photoconductive material, namely, LT-GaAs, radiating into a SI lens. Fig. 6(a) shows the layer structure of the chip. Starting from the side of the metallization, we find 2 μm of LT-GaAs, 400 nm of AlGaAs with 0.75% aluminum content, 200 nm of GaAs buffer, a 525 μm-thick SI-GaAs wafer. The metallization pattern of the antenna follows a bow-tie geometry [see Fig. 6(b)] with 45° taper angle and a square gap of $W_x = W_y = 10$ μm. A hemispherical SI lens with radius $R_{\text{lens}} = 10$ mm and extension length $E_{\text{lens}} = 0.29R_{\text{lens}}$ is placed on top of the bow-tie slot. The lens, see Fig. 7 for an impression, is coated with a quarter-wavelength matching layer (at a frequency of 0.4 THz) in order to reduce the reflection at the lens–air interface. This matching layer is made with a 114 μm-thick c-parylene coating with a relative permittivity of $= 2.72$ [18]. More details about the design, fabrication, and assembly of this device are thoroughly detailed in [12]. The material properties of the LT GaAs were included in Table I.

B. Experimental Setups

Two different setups are adopted for the measurements as shown in Fig. 7(a) and (b), one for performing the power measurements) and a second one for performing the spectrum measurements, respectively. They are both based on the commercial system TERA K15 available from Menlo

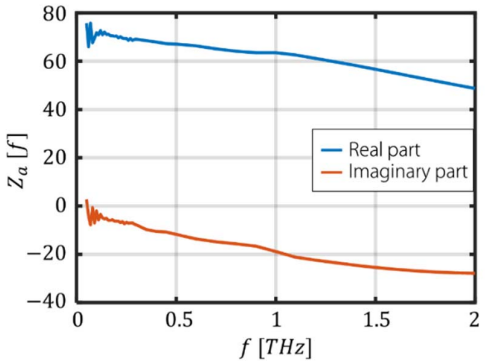

Fig. 5. Bow-tie antenna radiation impedance.

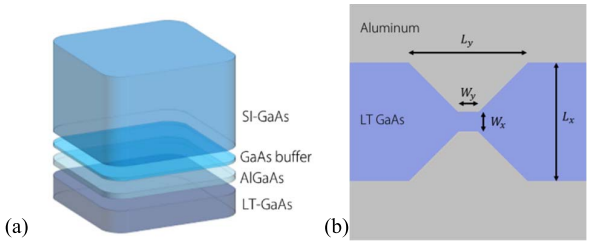

Fig. 6. (a) Dielectric stratification adopted for the device under investigation; the antenna is printed at the bottom side of the LT GaAs membrane. (b) Metallization bow-tie geometry printed over the photoconductor: W_x, W_y= 10 μm, L_x, L_y= 2 mm, and taper angle of 90°.

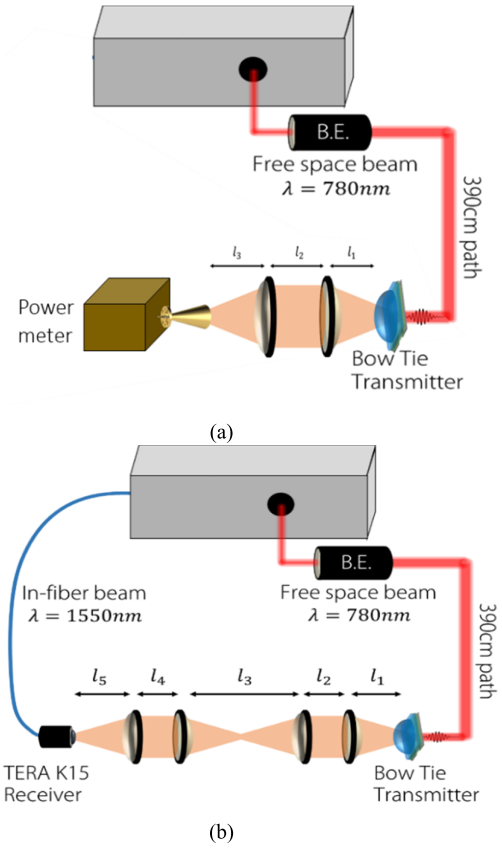

Fig. 7. Schematic of the two measurement setups where the transmitting bow-tie PCA is excited by the free-space laser. (a) Power measurements: the RX is a power meter coupled to a multimode horn via a couple of planoconvex polymer lenses (l_1 = 35 mm, l_2 = 60 mm, and l_3 = 20 mm). (b) Spectrum measurements: the RX is the PCA antenna native of the MENLO system excited by an in-fiber laser. A free-space delay line of 390 cm ensures the synchronization of the two PCA antennas. In this case, the quasi-optical path is composed of four identical planoconvex polymer lenses (l_1 = 20 mm, l_2 = 100 mm, l_3 = 90 mm, l_4 = 100 mm, and l_5 = 25 mm).

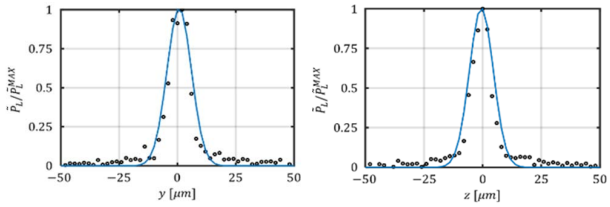

Fig. 8. Profile of the focused optical beam obtained with the setup in Fig. 7 along the vertical (y) and horizontal (z) axes. The blue solid line is a Gaussian fit to verify the gaussicity of the focused beam. The −3 dB diameter of the beam along the y-axis is D_L = 10.2 μm, and on the z-axis, it is D_L = 9.5 μm.

Systems [19], with ad hoc modifications. Specifically, the standard TX is replaced by the bow tie under investigation, which is fed by the free-space optical delay line shown in Fig. 7. The TX PCA is biased to a fixed voltage, V_b, which accelerates the photocarriers injected by the free-space laser source, $\lambda = 780$ nm.

The two experimental setups, however, use a different RX. A power meter (Virginia Diodes, PM5), as shown in Fig. 7(a), is used to characterize the THz power emitted by the bow-tie antenna. Instead, the RX from the TERA K15, Fig. 7(b), is used to measure the frequency response. The RX's lens antenna is the native Auston switch adopted by the TERA K15, fed by in-fiber optical pulses, $\lambda = 1550$ nm. Both lasers are pulsed at $f_L = 80$ MHz. The main difference between the power and frequency response setups (apart from the different RX) is the QO path used to couple the radiated signal with the RX. In both cases, the desire was the optimization of the coupling between the sources and the RXs.

In the power measurement setup, the THz signal is radiated by the antenna through a QO path consisting of two planoconvex polymer lenses (ThorLabs, TPX50) and is then coupled to a multimode conical horn antenna (Virginia Diodes, conical horn antenna CH-WR10) placed in front of the power meter. This QO setup has been designed in detail and its efficiency could be modeled to accuracies below 1 dB.

We also tried to optimize the coupling from our sources to TERA K15. To this goal, four identical planoconvex polymer lenses (ThorLabs TPX50) are used to collect the TX radiation and couple it to the RX from the TERA K15. However, the transition between the TERA K15 lens and the Auston switch in the focal plane of the lens is not known and could not be optimized.

The synchronization between the TX bow-tie and the RX MENLO antennas is achieved through a 390 cm optical delay path such that the RX is excited by the in-fiber laser when the field radiated by the TX antenna impinges on it. Finally, the photocurrent induced in the RX is sent to a transimpedance amplifier and processed by the read-out electronics. The temporal evolution of the THz pulse is recovered through

a stroboscopic sampling technique, where the reciprocal delay between the two laser sources is modulated by an optical delay unit (ODU) controlled electronically. The laser sources, the read-out electronics, as well as the ODU are part of TERA K15. The 390cm optical path is achieved through five flat protected gold mirrors (ThorLabs, PF05-03-M01), a beam expander (ThorLabs, BE02-05-B), and a focusing lens (ThorLabs, LA4725-B-ML), all carefully aligned and mounted on the optical table where the TERA K15 is placed. The average optical power available from the pulsed laser ranges from $\tilde{P}_L = 1 \rightarrow 240$ mW. The maximum measured optical average power reaching the TX antennas after the path losses introduced by the optical delay line of 390 cm is measured at $\tilde{P}_L = 180$ mW, which is consistent with the nominal loss introduced by the mirrors, beam expander, and focusing lens.

The laser delay line is built as follows. The beam emerges with a $1/e$ waist of $w_0 = 0.6$ mm and is ideally focused down to a waist of $w_L = 8.5$ μm (which corresponds to a -3 dB radius of $r_L^{-3\text{dB}} = 5$ μm or diameter of $D_L = 2r_L^{-3\text{dB}} = 10$ μm) to match the PC gap lateral dimensions $W_x, W_y = D_L$, ideally. A beam expander with a factor $5\times$ magnification is placed at the beginning of the delay line to avoid the divergence of the beam over the 390 cm optical path. The lens focusing the optical beam onto the antenna gap is a fused silica planoconvex lens with a diameter of 25.4 mm and a focal length of 75 mm. We profile the focused beam on both the horizontal and vertical axes using two metal blades and the knife-edge technique [20] to verify the laser spot size and the alignment of all the components in the delay line. The blades are placed in a holder controlled by a five-axis (three translational and two rotational axes) motorized stage with a translational resolution of $\delta_t = 1.25$ μm and a rotational resolution of $\delta_r = 0.01°$. The holder of the blade is the same one used for the antenna, thus ensuring that the measured profile is eventually the same exciting as the investigated PCA. The -3 dB diameter of the beam along the two orthogonal axes are 10.2 and 9.5 μm, and the results are shown in Fig. 8. The measured spillover efficiency is $\eta_{\text{so},y} = 0.58$ on the vertical axis and $\eta_{\text{so},z} = 0.59$ on the horizontal axis.

It should be noted that $\eta_{\text{so}} = 0.58$ guarantees an essentially uniform optical field distribution in the gap. The optical efficiency η_{opt} is discussed in the Appendix. For the measurements in this article, the total efficiency results in $\eta_{\text{opt}} = 0.35$.

C. Detected Power

Once the desired optical beam profile on the focal plane is achieved and its center position is found, the blades are replaced with the photoconductive bow-tie antenna. The holder of the bow-tie antenna is identical to one of the blades and ensures that the gap of the PCA is located at the center of the measured beam profile. The gap of the bow tie is a few tens of micrometers from the center of the focused laser spot due to the machining tolerance of the different holders and the mounting procedure [12]. Therefore, we fine-tune the device position of the bow tie (mounted in the five-axis motorized stage) in order to achieve the maximum gap illumination. The fine-tuning is performed by measuring the dc current induced in the gap excited by the laser and maximizing it with micrometric position adjustments. Fig. 9 shows the value of the measured dc current as a function of the incident laser average power $\tilde{P}_L$ with the PCA at the fine-tuned position. The position of the two lenses and the horn of the QO path are fine-tuned until the maximum power is detected by the power meter.

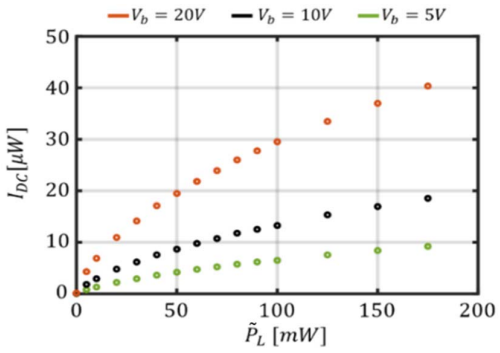

Fig. 9. Measured dc current with the beam obtained in Fig. 10 as a function of the laser power for three bias points: $V_b = 5$, 10, and 20 V.

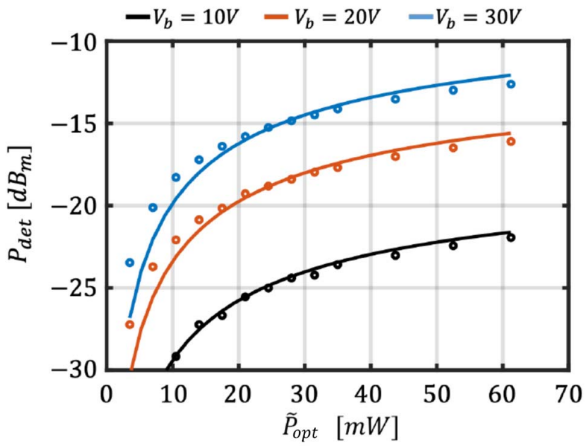

Fig. 10. Power detected by the power meter for three different bias levels as a function of the optical power absorbed in the gap. The dotted points represent the measurements, while the lines correspond to the simulations.

The THz power received is characterized versus the voltage biased stepped at $V_b = 10, 20,$ and 30 V. Fig. 10 shows the average THz power detected, $\tilde{P}_{\text{det}}$, as a function of the laser power absorbed by the PCA gap, $\tilde{P}_{\text{opt}} = \eta_{\text{opt}}\tilde{P}_L$, for the three different bias points. The power was measured by the PM5 power meter, based on a waveguide, used in over mode. As expected, the increase of the average power of the pulsed laser does not lead to a corresponding quadratic increase of the THz power. For larger optical excitations, the saturation effect appears.

In order to provide a theoretical prediction of the detected power, the coupling efficiency of the QO (THz) path is simulated with an in-house tool [21] alongside with Ticra GRASP [22], while the PCA beam pattern is computed and imported from the full-wave EM software CST [17].

Fig. 11 shows the efficiency of the QO channel with the optimum positions found during the power

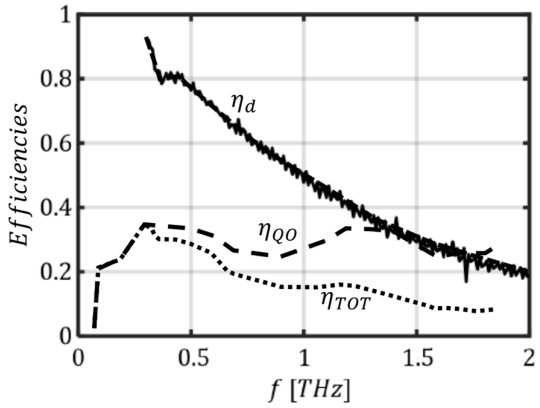

Fig. 11. Simulated total efficiency (dotted line) as the product of dielectric loss efficiency (solid line) and quasi-optical channel efficiency (dashed line).

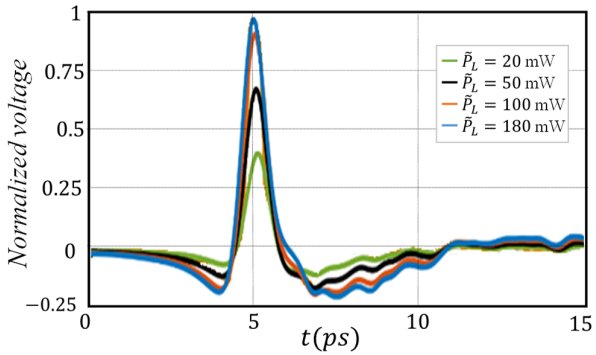

Fig. 12. Measured time-domain pulses radiated by the bow tie under investigation and collected by the RX native of the TERA K15: the TX antenna is biased at $V_b = 30$ V and excited by different levels of average optical power reaching the antennas (see the inset).

measurements, defined as $\eta_{\rm QO}(f) = E_{\rm det}(f)/E_{\rm rad}(f)$, as a function of the frequency. $E_{\rm rad}(f)$ was estimated in (15). Different loss mechanisms and the corresponding efficiencies of the QO channel were discussed in [20] and are also provided. With reference to Fig. 7(b), the most important of these mechanisms are the reflections at the dielectric–air interface in the transmitting antenna, the spillover that the field radiated by the first lens antenna encounter in the dual lens channel and, finally, the mismatch between the field exiting the final lens and the multimode power meter waveguide horn: eventually, all these three causes contribute to the QO efficiency $\eta_{\rm QO}(f)$. The frequency oscillation in $\eta_{\rm QO}(f)$ is the result of the adoption of a single matching layer that is tuned to maximize the efficiency at 400 GHz. Overall, the QO channel provides an average efficiency of $\eta_{\rm QO}^{\rm ave} \simeq 0.27$, for frequencies higher than the cutoff (75 GHz) introduced by the waveguide of the power meter. The QO efficiency must be complemented with the dielectric losses in the lenses, η_d, as shown in Fig. 11. These latter lenses were directly provided by the MENLO systems. Fig. 11 eventually shows, in a dotted line, the total efficiency, $\eta_{\rm TOT}$, expected to be representing the transfer of spectral energy from the bow feed to the power meter.

The average power detected at the power meter can also be estimated as

$$\tilde{P}_{\rm det} = \frac{2}{T}\int_0^\infty Re\{Z_a(f)\}|I(f)|^2\eta_{\rm TOT}(f)df. \qquad (17)$$

The estimated detected THz power as a function of the total average laser power absorbed by the device is also shown in Fig. 10 for the three different bias levels, $V_b = 10$, 20, and 30 V. The measured power for the three different voltages is fit with our model, where the only fitting parameter is the scattering time, τ_s.

It turns out that $\tau_s = 8.5$ fs provides the best fit between the measured data and our model. This number is within the order of the values that have been observed in [3]. The agreement is exceptional, and the differences between the data and the model are within only 1 dB. The saturation effect occurring at large optical power levels observed in the measurement emerges also clearly from the model. The saturation to the screening induced over the gap by the field radiated by the PCA can thus be simply attributed to the feedback of the antenna on the bias.

D. Spectral Response

After having characterized the radiated power, the signal spectra are acquired by resorting to the THz pulses measured with the complete setup in Fig. 7(a). Fig. 12 shows the THz pulses received by the RX module of the TERA K15 with the TX biased at $V_b = 30$ V and excited by different optical pulses ranging from $\tilde{P}_L = 20$ to 180 mW.

The received signals are normalized to the maximum received since the MENLO RX is not absolutely calibrated. However, the relative differences are of interest. Stronger responses are clearly visible for higher optical excitations. A close look also suggests some variation of the temporal evolution of the received signal and, consequently, its frequency behavior. Note that with the bow tie under investigation excited by $P_L = 30$ mW and biased at $V_b = 30$ V, we receive about $P_{\rm det} = 15$ μW (see Fig. 10).

The corresponding spectra, also normalized to the maximum value observed, are evaluated by performing the Fourier transforms of the signals of Fig. 12 and are shown in Fig. 13. The spectra detected using the bow-tie PCA as a TX present stable behavior, with sharp absorption lines given by the water content in the air. The strong oscillations observable at very low frequencies are induced by the RX Auston switch antenna, which does not radiate efficiently before $f \simeq 100$ GHz. A careful observation of the inset of Fig. 13 shows that for higher optical excitations, the largest increases in power occur at the lower frequencies, while only moderate enhancements emerge for the higher spectral components.

Fig. 14 compares the difference between the spectra at high ($\tilde{P}_L = 180$ mW) and low ($\tilde{P}_L = 20$ mW) optical powers. Specifically, the measurement curves refer to

$$\frac{E_f^{\rm meas}(\tilde{P}_L = 20\ {\rm mW})}{E_{\rm 50GHz}^{\rm meas}(\tilde{P}_L = 20\ {\rm mW})} - \frac{E_f^{\rm meas}(\tilde{P}_L = 180\ {\rm mW})}{E_{\rm 50GHz}^{\rm meas}(\tilde{P}_L = 180\ {\rm mW})} \qquad (18a)$$

while the simulation curves present

$$\frac{E_f^{\rm rad}(\tilde{P}_L = 20\ {\rm mW})}{E_{\rm 50GHz}^{\rm rad}(\tilde{P}_L = 20\ {\rm mW})} - \frac{E_f^{\rm rad}(\tilde{P}_L = 180\ {\rm mW})}{E_{\rm 50GHz}^{\rm rad}(\tilde{P}_L = 180\ {\rm mW})} \qquad (18b)$$

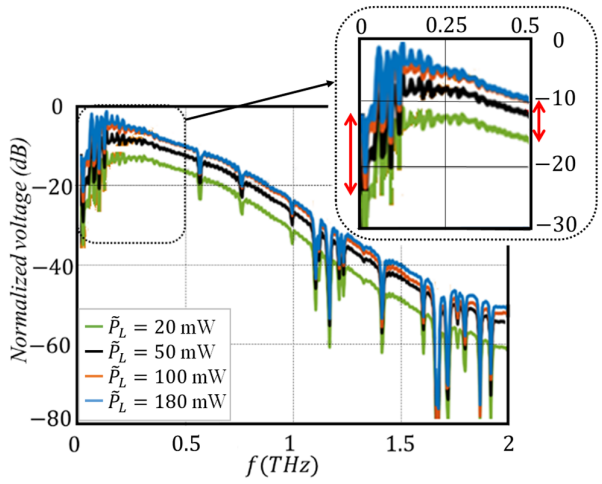

Fig. 13. Spectra of the measured time-domain pulses radiated by the bow tie under investigation and collected by the RX native of the TERA K15: the TX antenna is biased at $V_b = 30$ V and excited by different levels of optical power (see inset). The inset of this figure shows that for higher optical excitations, the largest increases in power occur at the lower frequencies, whereas only moderate enhancements emerge for the higher spectral components.

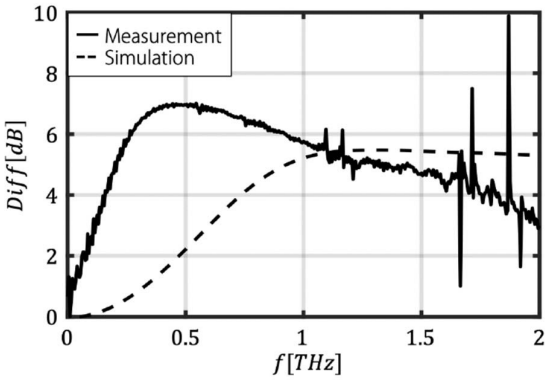

Fig. 14. Energy spectra radiated by the antenna evaluated using the methodology presented in this article opposed to the acquired measurements for two different excitation levels as a function of the frequency: normalized spectra at their maximum value.

where $E_f^{\text{rad}}(P_l)$ is the simulated spectral energy radiated in an infinite SI medium, i.e., the entire QO channel is not modeled in these results. The normalization of both spectra is at 50 GHz. As expected, the higher frequency components due to lower optical powers appear larger in both simulations and measurements. The fact that this frequency trend is similar in simulations and measurements can be interpreted as comforting. The circuit model predicts well that there is comparatively less power at high frequencies when exciting the structure with higher optical powers.

One might observe that the largest disagreements between simulation and measurement in Fig. 14 appear below one 700 GHz. This is because our model only accounts for the power generated by the bow-tie antenna and does not model the Menlo system receive path. The Menlo system is unfortunately inaccurate in representing the spectrum of a singly polarized signal (as the one radiated by the bow-tie antenna). This is because it uses an Auston switch radiating structure. The low-frequency radiation from an Auston switch is due to the feeding lines, and this radiation is polarized orthogonally to the field radiated by the central dipole, which becomes dominant above 700 GHz. At higher frequencies, the predictions and the measurements tend to agree up to 2THz when the measured signal approaches the noise floor of the system.

IV. Conclusion

This contribution first provides the components for the Norton equivalent circuit in time domain that characterizes pulsed, LT GaAs-based, broadband PCA. The circuit is then solved, following a stepped time evolution, to derive the electric current characterizing the THz pulses radiated by the antenna. In the particular case that the antenna feeds a dielectric lens, the antenna radiation impedance, and its beam pattern within and outside the lens are then simulated by resorting to in-house tools combined with commercially available EM modeling software. Finally, the entire QO channel from TX to RX is simulated to represent the available measurement setup.

The predicted results in terms of power generated and spectral responses are then compared with measured results for a standard bow-tie-based PCA system. The experimental validation shows that the described modeling procedure is efficient and accurate to obtain the temporal evolution of the induced photocurrent and its spectrum, as well as the power radiated with the THz beam for broadband PCA excited by pulsed lasers. The saturation of the radiated power observed under large optical excitations as predicted by the model shows an excellent agreement with the measurements.

This agreement, obtained without requiring fine-tuning from the measurements, demonstrates a significant improvement of the modeling now available [10]. The level of accuracy of the modeling introduced with this contribution is now comparable to that expected in nonpulsed heterodyne systems and opens new opportunities to engineer much more advanced front ends, which will be in the end limited by the quality of the antenna designs.

Appendix A
Amplitude of the Laser Source

The temporal evolution of the carrier density function in the active portion of a photoconductor depends on the characteristics of the laser exciting the volume as well as the properties of the material: both are described in Table I. Also, in [11], reference was made to optical power exciting the gap. In modeling the present experiment, the general term optical power $\tilde{P}_{\text{opt}}$ used in [11] indicates the power actually absorbed in the PC gap. Following a procedure similar to the one presented in [12], the generation of charge particles induced at every point, $\vec{\rho}, z$, with the PC material of Fig. 1 by

modulated laser pulses, can be expressed as

$$g_{\text{gen}}(t,\vec{\rho},z)=\frac{P_0 e^{-4ln2\frac{t^2}{\tau_p^2}}}{hf_c}\left(1-|\Gamma|^2\right)\frac{e^{-\frac{\rho^2}{2\pi\sigma_\rho^2}}}{2\pi\sigma_\rho^2}\frac{d}{dz}e^{-\frac{|z|}{\alpha}} \tag{A-1}$$

$$P_0=\tilde{P}_L\frac{T}{\tau_p}\sqrt{\frac{4ln2}{\pi}}\text{(A2)} \tag{A-2}$$

where $\rho=x\hat{x}+y\hat{y}$ is the observation point in the horizontal plane $z=0$, P_0 is the laser peak power (incident on the PCA focal region), $\tilde{P}_L$ is the laser average power (also incident on the PCA), $\Gamma=(0.3)^{1/2}$ is the plane wave reflection coefficient between free space and LT GaAs, $\sigma_\rho=(D_L/2(2ln2)^{1/2})$, D_L is the laser beam Poynting vector -3 dB diameter, and $\alpha=1\ \mu$m is the absorption length in z for a plane wave at the carrier frequency. The carrier generation function is different for every observation point $(\vec{\rho},z)$; thus, in order to simplify the analysis and get rid of the spatial dependence, it is convenient to average the generation function in the whole active volume

$$\begin{aligned}\bar{g}_{\text{gen}}(t)&=As_n(t)\\&=\frac{1}{\text{Vol}}\int_{-\frac{W_x}{2}}^{\frac{W_x}{2}}\int_{-\frac{W_y}{2}}^{\frac{W_y}{2}}\int_{-W_z}^{0}g_{\text{gen}}(t,\vec{r})dzdydx=\end{aligned} \tag{A-3}$$

where

$$\text{Vol}=W_xW_yW_z,\ s_n(t)=e^{-4ln2\frac{t^2}{\tau_p^2}}. \tag{A-4}$$

The amplitude A includes all the integral geometrical effects and well as the bulk properties of the PC material. In order to obtain a more compact expression for the amplitude, A, it is convenient to compactly indicate the integration in x and y as spillover efficiency η_{so}

$$\eta_{\text{so}}=\int_{-\frac{W_x}{2}}^{\frac{W_x}{2}}\int_{-\frac{W_y}{2}}^{\frac{W_y}{2}}\frac{e^{-\frac{\rho^2}{2\pi\sigma_\rho^2}}}{2\pi\sigma_\rho^2}dydx \tag{A-5}$$

and to introduce the optical efficiency, η_{opt}, as

$$\eta_{\text{opt}}=\eta_{\text{so}}\left(1-|\Gamma|^2\right)\left(1-e^{-\frac{w_z}{\alpha}}\right) \tag{A-6}$$

so that the amplitude can be expressed as

$$A=\eta_{\text{opt}}\frac{\tilde{P}_L}{hf_c}\frac{T_L}{\tau_p}\sqrt{\frac{4ln2}{\pi}}\frac{1}{\text{Vol}}. \tag{A-7}$$

The absorbed power in the gap would then be indicated as

$$\tilde{P}_{\text{opt}}=\eta_{\text{opt}}\tilde{P}_L. \tag{A-8}$$

REFERENCES

[1] D. H. Auston, K. P. Cheung, and P. R. Smith, "Picosecond photoconducting Hertzian dipoles," *Appl. Phys. Lett.*, vol. 45, no. 3, pp. 284–286, May 1984.

[2] D. Grischkowsky, S. Keiding, M. van Exter, and C. Fattinger, "Far-infrared time-domain spectroscopy with terahertz beams of dielectrics and semiconductors," *J. Opt. Soc. Amer. B, Opt. Phys.*, vol. 7, no. 10, pp. 2006–2015, Oct. 1990.

[3] P. U. Jepsen, R. H. Jacobsen, and S. R. Keiding, "Generation and detection of terahertz pulses from biased semiconductor antennas," *J. Opt. Soc. Amer. B, Opt. Phys.*, vol. 13, no. 11, pp. 2424–2436, Nov. 1996.

[4] S. Verghese, K. A. McIntosh, and E. R. Brown, "Highly tunable fiber-coupled photomixers with coherent terahertz output power," *IEEE Trans. Microw. Theory Techn.*, vol. 45, no. 8, pp. 1301–1309, Aug. 1997.

[5] S. D. Brorson, J. Zhang, and S. R. Keiding, "Ultrafast carrier trapping and slow recombination in ion-bombarded silicon on sapphire measured via THz spectroscopy," *Appl. Phys. Lett.*, vol. 64, no. 18, pp. 2385–2387, May 1994.

[6] M. Tani, S. Matsuura, K. Sakai, and S. Nakashima, "Emission characteristics of photoconductive antennas based on low temperaturegrown GaAs and semi-insulating GaAs," *Appl. Opt.*, vol. 36, no. 30, pp. 7853–7859, Oct. 1997.

[7] Z. Piao et al., "Carrier dynamics and terahertz radiation in photoconductive antennas," *Jpn. J. Appl. Phys.*, vol. 39, pp. 96–100, Jan. 2000.

[8] J. Karsten Siebert et al., "Field screening in low temperature grown GaAs photoconductive antennas," *Jpn. J. Appl. Phys.*, vol. 43, no. 3, pp. 1038–1043, 2004.

[9] G. C. Loata, M. D. Thomson, T. Löffler, and H. G. Roskos, "Radiation field screening in photoconductive antennae studied via pulsed terahertz emission spectroscopy," *Appl. Phys. Lett.*, vol. 91, Dec. 2007, Art. no. 232506.

[10] O. A. Castañeda-Uribe, C. A. Criollo, S. Winnerl, M. Helm, and A. Avila, "Comparative study of equivalent circuit models for photoconductive antennas," *Opt. Exp.*, vol. 26, no. 22, pp. 29017–29031, 2018.

[11] A. Neto, N. Llombart Juan, and A. Freni, "Time-domain modelling of pulsed photoconducting sources—Part I: The Norton equivalent circuit," *IEEE Trans. Antennas Propag.*, vol. 71, no. 3, pp. 2527–2535, Mar. 2023.

[12] A. Garufo, G. Carluccio, N. Llombart, and A. Neto, "Norton equivalent circuit for pulsed photoconductive antennas—Part I: Theoretical model," *IEEE Trans. Antennas Propag.*, vol. 66, no. 4, pp. 1635–1645, Apr. 2018.

[13] A. F. Bernardis, "On the modelling and characterisation of photoconducting antennas," Ph.D. dissertation, Dept. Microelectronics, THz Sensing Group, Delft Univ. Technol., Delft, The Netherlands, 2022.

[14] P. Drude, "Zur Elektronentheorie der Metalle," *Annalen der Physik*, vol. 306, Mar. 1900, Art. no. 566613.

[15] D. R. Grischkowsky, "Nonlinear generation of sub-psec pulses of THz electromagnetic radiation by optoelectronics—Application to time-domain spectroscopy," in *Frontiers in Nonlinear Optics*, H. Walther, N. Koroteev, and M. O. Scully, Eds. Philadelphia, PA, USA: Institute of Physics, 1993.

[16] J. Shan and T. F. Heinz, "Terahertz radiation from semiconductors," in *Ultrafast Dynamical Processes in Semiconductors*, vol. 92, K.-T. Tsen, Ed. Berlin, Germany: Springer-Verlag, 2004, pp. 1–59.

[17] *CST Microwave Studio*. Accessed: 2022. [Online]. Available: http://www.cst.com

[18] *Specialty Coating Systems*. Accessed: 2023. [Online]. Available: https://scscoatings.com

[19] *Menlo System*. Accessed: 2023. [Online]. Available: https://www.menlosystems.com

[20] A. Garufo, "Towards the engineering of pulsed photoconductive antennas," Ph.D. dissertation, Dept. Microelectronics, THz Sensing Group, Delft Univ. Technol., Delft, The Netherlands, 2017.

[21] H. Zhang, S. O. Dabironezare, G. Carluccio, A. Neto, and N. Llombart, "A Fourier optics tool to derive the plane wave spectrum of quasi-optical systems [EM programmer's notebook]," *IEEE Antennas Propag. Mag.*, vol. 63, no. 1, pp. 103–116, Feb. 2021.

[22] TICRA. *TICRA Tools 20.0*. Accessed: 2022. [Online]. Available: https://www.ticra.com/software/grasp

Arturo Fiorellini Bernardis (Graduate Student Member, IEEE) received the B.Sc. degree in biomedical engineering from the Politecnico di Milano, Milan, Italy, in 2014, and the M.Sc. degree (cum laude) in electrical engineering from the Delft University of Technology (TU Delft), Delft, The Netherlands, in 2017, where he is currently pursuing the Ph.D. degree with the Terahertz Sensing Group, Department of Microelectronics.

His research interests include electromagnetic theory as well as the analysis and design of photoconductive antennas for security applications.

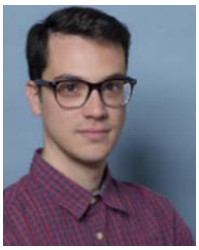

Paolo Maria Sberna was born in Palermo, Italy, in 1987. He received the bachelor's degree (cum laude) in physics from the University of Catania, Catania, Italy, in 2009, with a thesis on Bose–Einstein condensation, the master's degree (cum laude) in physics from the University of Catania, in 2011, with the thesis Quantum confinement effects on Si nanocrystals observed with Raman spectroscopy, and the Ph.D. degree from the University of Catania and partly from the NOVA University of Lisbon, Lisbon, Portugal, in 2015, with the thesis novel approaches to photoactive nanostructured materials for efficient solar cells.

Since May 2015, he has been with the Delft University of Technology (TU Delft), Delft, The Netherlands. The topic covered during the first two years has been low-temperature Si thin-film transistors fabrication by solution processing. Since 2017, he has been working on III–V photoconductive antennas for terahertz (THz) applications with the Terahertz Sensing Group, Microelectronic Department, TU Delft. Since September 2018, he has been Equipment Responsible Scientist with the Else Kooi Laboratory, TU Delft. His research interests are solid-state physics, material science, chemistry, and microfabrication.

Juan Bueno received the graduate degree in physics from the University of Cantabria, Santander, Spain, in 2003, and the Ph.D. degree from the University of Leiden, Leiden, The Netherlands, in 2007.

During his Ph.D. degree studies, he studied quantum crystals at very low temperatures. From 2007 to 2008, he was a Post-Doctoral Fellow with the University of California, San Diego, CA, USA, continuing his work on quantum crystals. In 2008, he made the decision to switch research topics and interests from fundamental physics to the study of superconducting devices. He was awarded with a NASA Post-Doctoral Position (NPP), becoming a Postdoc with the Jet Propulsion Laboratory, Pasadena, CA, USA, until 2010. During this time, he pioneered a new type of pair-breaking radiation detector, the Quantum Capacitance Detector. After his time with JPL, he joined the Center for Astrobiology, Torrejón de Ardoz, Spain, in 2010, after receiving a JAE-doc grant, working mainly on kinetic inductance detectors (KIDs). He became an Instrument Scientist with SRON—Netherlands Institute for Space Research, Leiden, in 2012, working on the development of KIDs for sub-millimeter wave and far IR space-based observatories. He has published more than 30 peer-reviewed articles, a third of them as the first author. His research interests concentrate on the development of ultrasensitive broadband KIDs for future space-based missions.

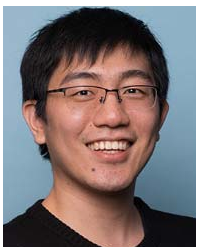

Huasheng Zhang (Graduate Student Member, IEEE) received the B.Eng. degree (cum laude) in electronic information engineering from Beihang University, Beijing, China, in 2016, and the M.Sc. degree (cum laude) in electrical engineering from the Delft University of Technology (TU Delft), Delft, The Netherlands, in 2018, where he is currently pursuing the Ph.D. degree with the Terahertz Sensing Group.

His research interests include the design of quasi-optical (QO) systems and antenna feeds for next-generation communication and sensing systems.

Nuria Llombart (Fellow, IEEE) received the master's degree in electrical engineering and the Ph.D. degree from the Polytechnic University of Valencia, Valencia, Spain, in 2002 and 2006, respectively.

During her master's degree studies, she spent one year at the Friedrich-Alexander University of Erlangen-Nuremberg, Erlangen, Germany, and worked at the Fraunhofer Institute for Integrated Circuits, Erlangen. From 2002 to 2007, she was with the Antenna Group, TNO Defense, Security and Safety Institute, The Hague, The Netherlands, working as a Ph.D. student and afterward as a Researcher. From 2007 to 2010, she was a Post-Doctoral Fellow with the California Institute of Technology, Pasadena, CA, USA, working with the Submillimeter Wave Advance Technology Group, Jet Propulsion Laboratory, Pasadena. She was a "Ramón y Cajal" Fellow with the Department of Optics, Complutense University of Madrid, Madrid, Spain, from 2010 to 2012. In September 2012, she joined the THz Sensing Group, Delft University of Technology, Delft, The Netherlands, where she has been a Full Professor since February 2018. She has coauthored more than 150 journal and international conference contributions. Her research interests include the analysis and design of planar antennas, periodic structures, reflector antennas, lens antennas, and waveguide structures, with an emphasis on the THz range.

Dr. Llombart serves as a Board Member for the IRMMW-THz International Society. She was a recipient of the H. A. Wheeler Award for the Best Applications Paper of 2008 in the IEEE TRANSACTIONS ON ANTENNAS AND PROPAGATION, the 2014 THz Science and Technology Best Paper Award of the IEEE Microwave Theory and Techniques Society, the 2014 IEEE Antenna and Propagation Society Lot Shafai Mid-Career Distinguished Achievement Award, the European Research Council Starting Grant in 2015, and several NASA awards.

Andrea Neto (Fellow, IEEE) received the Laurea degree (summa cum laude) in electronic engineering from the University of Florence, Florence, Italy, in 1994, and the Ph.D. degree in electromagnetics from the University of Siena, Siena, Italy, in 2000.

Part of his Ph.D. degree was developed at the European Space Agency Research and Technology Center, Noordwijk, The Netherlands. He worked at the Antenna Section, European Space Agency Research and Technology Center, for over two years. From 2000 to 2001, he was a Post-Doctoral Researcher with the California Institute of Technology, Pasadena, CA, USA, where he worked at the Submillimeter Wave Advanced Technology Group. From 2002 to January 2010, he was a Senior Antenna Scientist with TNO Defense, Security, and Safety, The Hague, The Netherlands. In February 2010, he became a Full Professor of applied electromagnetism at the Department of Electrical Engineering, Mathematics and Computer Science, Delft University of Technology, Delft, The Netherlands, where he formed and leads the THz Sensing Group. His research interests include the analysis and design of antennas with an emphasis on arrays, dielectric lens antennas, wideband antennas, EBG structures, and THz antennas.

Dr. Neto is a member of the Technical Board of the European School of Antennas and an organizer of the course on antenna imaging techniques. He is also a member of the Steering Committee of the Network of Excellence NEW-FOCUS, dedicated to focusing techniques in millimeter and sub-millimeter-wave regimes. He was a recipient of the European Research Council Starting Grant to perform research on advanced antenna architectures for THz sensing systems in 2011, the H. A. Wheeler Award for the best applications paper of 2008 in the IEEE TRANSACTIONS ON ANTENNAS AND PROPAGATION, the Best Innovative Paper Prize of the 30th ESA Antenna Workshop in 2008, and the Best Antenna Theory Paper Prize of the European Conference on Antennas and Propagation (EuCAP) in 2010. He served as an Associate Editor for the IEEE TRANSACTIONS ON ANTENNAS AND PROPAGATION from 2008 to 2013 and IEEE ANTENNAS AND WIRELESS PROPAGATION LETTERS from 2005 to 2013.